

1
2 Investigating the Impact of Saharan Dust Aerosols on Analyses and Forecasts of African
3 Easterly Waves by Constraining Aerosol Effects in Radiance Data Assimilation
4
5
6
7

8 By

9 Dustin F. P. Grogan¹

10 Cheng-Hsuan Lu^{1,2}

11 Shih-Wei Wei^{1,2}

12 Sheng-Po Chen^{1,3}
13

14 1. University at Albany, State University of New York, Albany, NY

15 2. Joint Center for Satellite Data Assimilation, Boulder, CO

16 3. Department of Chemistry, National Central University, Taoyuan, Taiwan
17

18
19 Submitted to

20
21 Atmospheric Chemistry and Physics
22

23 on
24

25 February 15th, 2021
26

27 Revised on
28

29 October 13th, 2021
30
31
32

33 Corresponding author: Dustin Grogan, University at Albany, 1400 Washington Ave, Albany, NY
34 12222; dgrogan@albany.edu

35 **Abstract:**

36 This study incorporates aerosol effects into satellite radiance calculations within the
37 Global Data Assimilation System (GDAS) to investigate its impact on the analyses and forecasts
38 of African easterly waves (AEWs). A comparison of analysis fields from the aerosol-aware
39 assimilation experiment and an aerosol-blind control during August 2017 resulted in a warmer
40 Saharan boundary layer; a faster African easterly jet; and AEWs with enhanced northern tracks
41 and reduced southern tracks. The changes to the tracks are qualitatively consistent with
42 arguments of baroclinic and barotropic instability. During the time period, we examined two
43 AEWs that developed Hurricane Gert (2017) and Harvey (2017) over the Atlantic, but were
44 structurally different over Africa; the AEW for Gert consisted of a southern circulation, while the
45 AEW for Harvey consisted of a northern and southern circulation. Analysis differences of the
46 cases showed stronger vorticity changes for the AEW that developed Harvey, which we attribute
47 to the aerosol-aware assimilation capturing dust radiative effects involving a large-scale Saharan
48 dust plume that interacted with the AEW's northern circulation. Forecasts from the Global
49 Forecast System (GFS, v14) initialized by the different GDAS analyses for the AEW cases
50 showed that the aerosol-aware experiment reduced errors in the downstream vorticity for the
51 AEW that developed Harvey; neutral improvement was found for the AEW that develop Gert.
52 Thus, aerosol-affected radiances in the assimilation system have the ability to correct analysis
53 fields to account for the dust radiative effects on AEWs, which in turn can improve forecasts of
54 the AEWs as they travel downstream.

55

56

57

58

59 **1. Introduction**

60 In regions around the world, aerosols can have a profound impact on weather. This is
61 especially the case over North Africa as it houses the Saharan Desert, which is the largest emitter
62 of mineral dust aerosols, and African Easterly Waves (AEWs), which are synoptic-scale
63 circulation systems.

64 AEWs are the dominant synoptic-scale disturbance over North Africa from March to
65 October (Carlson 1969; Burpee 1972). The waves develop along the African easterly jet (AEJ),
66 which is a tropospheric jet (~650 hPa) whose axis is centered in the Sahel (~15°N). The AEWs
67 are also maintained by the AEJ through barotropic and baroclinic energy conversions. (Norquist
68 et al. 1977). Consequently, the AEWs can have two cyclonic circulations that reside on either
69 side of the AEJ axis (Reed et al. 1988; Pytharilous and Thorncroft 1999). The circulation south
70 of the AEJ peaks at ~650 hPa and is frequently coupled to moist convection (Kiladis et al. 2006;
71 Berry and Thorncroft 2005), while the northern circulation peaks at ~850 hPa, is dry, and can be
72 immersed in Saharan dust (Knippertz and Todd 2010; Grogan and Thorncroft 2019). Over the
73 East Atlantic, the two circulation centers often merge into a single circulation, which can
74 produce a favorable environment for tropical cyclogenesis (Schwendike and Jones 2010; Ross
75 and Krishnamurti 2007).

76 During summer, Saharan dust emissions are most active over the western Sahel (16°N-
77 24°N, 0°-15°W) (Cowie et al. 2014), the same region the AEW northern track resides. The
78 emissions are driven by enhanced surface winds that blow over dry and erodible regions (Tegan
79 and Fun 1994; Webb and Strong 2011). Once lifted, the dust mixes within the deep Saharan
80 boundary layer (Cuesta et al. 2009; Knippertz and Todd 2012) and can form plumes that span
81 thousands of kilometers. The transport of these large-scale dust plumes has been connected to

82 African easterly waves (Westphal et al. 1988; Jones et al. 2003; Knippertz and Todd 2010;
83 Nathan et al. 2019; Grogan and Thorncroft 2019). The dust can also be carried westward over the
84 Atlantic within the Saharan air layer (SAL) (Karyampudi et al. 1999; Chen et al. 2010), which is
85 an elevated layer of dry air that originates from the Saharan boundary layer.

86 Dust directly affects the scattering and absorption of incoming and outgoing radiation of
87 the atmosphere, which produces heating rates that can influence AEWs through two distinct
88 pathways (Bercos-Hickey et al. 2017). The first pathway is through the background (time-
89 averaged) dust fields, which produce heating rates that modify the background temperature and
90 wind fields (i.e., the AEJ), which in turn affects AEW structure and development (Jones et al
91 2004; Wilcox et al. 2010; Jury and Santiago 2010). The second pathway is through the formation
92 of large-scale episodic dust plumes, which produces heating rates that correlate with the wind
93 and temperature of the AEW to directly affect its growth rates, phase speeds, energetics, and
94 spatial structures (Grogan et al. 2016, 2017, 2019; Nathan et al. 2017).

95 To incorporate the above-mentioned dust radiative effects on AEWs within a numerical
96 weather prediction (NWP) system, it is important to represent the episodic nature of the aerosols.
97 These radiative effects have been included into NWP systems through two approaches: (i)
98 radiatively coupling aerosols in the forecast model, and (ii) incorporating aerosols in satellite
99 radiance calculations during data assimilation (DA).

100 For the first approach, aerosol attenuation modifies the heating rates within the radiation
101 schemes of the forecast model of the NWP system. Studies have shown that this improves the
102 forecast skill of several features in dust-affected regions over North Africa and the East Atlantic,
103 including sea-level pressure and atmospheric temperature (Perez et al. 2006; Mulcahy et al.
104 2014), AEWs linked to tropical cyclogenesis (Reale et al. 2009; Reale et al. 2011; Chen et al.

105 2015), and the AEJ (Reale et al. 2014). Major efforts are also ongoing to improve aerosol
106 prediction models, including the particle's emission and removal processes, assimilating
107 observations such as aerosol optical depth (AOD), and model verification and evaluation (see
108 Benedetti et al. (2018) for a comprehensive discussion). Such advances in aerosol prediction
109 models can, in turn, improve weather prediction. But despite these advances, the radiatively
110 coupling of episodic aerosols in the NWP system is often not feasible in an operational setting
111 due to computational costs. Thus, most operational NWP systems use prescribed aerosol
112 climatologies, such as the NCEP operational Global Forecast System (GFS; Hou et al. 2002) and
113 the ECMWF integrated forecast system (IFS; Bozzo et al. 2017). Consequently, the NWP system
114 sacrifices the ability to represent episodic aerosol signals.

115 For the second approach, aerosol transmittance effects are considered during radiance
116 DA, which modifies the analysis fields of the NWP system. Kim et al. (2018) demonstrated this
117 approach by including 3-hourly aerosol fields from the Goddard Chemistry Aerosol Radiation
118 and Transport (GOCART) model into the radiance calculations within the Goddard Earth
119 Observing System (GEOS)-atmospheric data assimilation system (ADAS). Kim et al. (2018)
120 showed that when aerosols were considered, they found the fit to observations improved for
121 satellite infrared (IR) sounders due to accounting for the aerosol transmittance effects in the form
122 of cooling brightness temperatures (BT), which has been observed in previous studies (e.g.,
123 Sokolik 2002). As a result, the cooling of BTs led to warmer analyzed surface temperatures in
124 the Tropical Atlantic. Similarly, Wei et al. (2020, 2021) showed that considering aerosol
125 transmittance effects warmed analyzed sea-surface temperatures and low-level air temperatures
126 over the transatlantic region and Africa when including aerosols from NOAA's Environmental
127 Modeling System (NEMS) GFS Aerosol Component (NGAC) into NCEP's global data

128 assimilation system (GDAS). Wei et al. (2020) also showed that the aerosols improved
129 forecasting of vector winds and geopotential heights at multiple levels in the tropical region from
130 the GFS model.

131 Incorporating aerosol transmittance effects into the radiance calculation of DA is
132 excluded from all NWP centers, despite its relatively low computation costs and its potential to
133 leverage aerosol-affected radiances in a physical and consistent way. But more studies
134 investigating this approach are needed. For example, no study has used this approach to examine
135 the impacts of dust radiative effects on AEWs in the NWP system. Motivated by the results in
136 Kim et. al. (2018) and Wei et al. (2020, 2021), along with the physical understanding of dust
137 radiative effects on AEWs identified in the literature, this study seeks to examine how, and to
138 what extent, episodic aerosols in the satellite radiance calculations can affect analyses and
139 forecasts of AEWs over North Africa and the East Atlantic. We focus our analysis on two AEWs
140 during August 2017 that are structurally different over North Africa but later developed
141 hurricanes over the Atlantic.

142 In Section 2, we describe the model experiments and the methods used to track the
143 AEWs. Section 3 presents the analysis differences and forecast performances from each
144 experiment and examines the analysis results from the aerosol-aware experiment in the context
145 of dust radiative effects on AEWs. Section 4 provides conclusions and a short discussion.

146 **2. Experiments and Methods**

147 *2.1 Model Experiments*

148 The schematic in Fig. 1 illustrates the workflow of the experiments in this study, which
149 were conducted from July 25th – August 28th, 2017. The first experiment is an aerosol blind run
150 (CTL), where aerosols are not considered in the assimilation system. The second experiment is

151 an aerosol-aware run (AER), which constrains aerosol transmittance effects into the radiance
152 calculations of the assimilation system (i.e., aerosol-affected radiances). For our experiments, we
153 employ version 14 of the National Centers for Environmental Prediction (NCEP) Global
154 Forecast System (GFS, v14), which consists of an analysis system, the Global Data Assimilation
155 System (GDAS), and a forecast model, the global spectral model (GSM), with GFS physics. The
156 experiments are fully-cycled, which means that each analysis is constructed from their respective
157 forecasts of the prior cycle.

158 The analyses are constructed using GDAS (Fig. 1: blue), which is a Gridpoint Statistical
159 Interpolation (GSI) based four-dimensional ensemble-variational (4DEnVar) assimilation
160 system. The assimilation system is run for 80 ensemble members at T254 (~80km) resolution. In
161 GDAS, the radiance calculations are conducted by the Community Radiance Transfer Model
162 (CRTM) (Lu et al. 2021). The CRTM generates simulated brightness temperatures (BT) and
163 computes the radiance sensitivities with respect to the state variables (Han et al. 2006).

164 For both experiments, various observations are ingested into GDAS, including the
165 conventional dataset (e.g., radiosondes, ships, buoys, etc.), and satellite observations (e.g.,
166 retrievals and radiances) (Fig. 1: gray). In particular, for the radiance observations, we include
167 the level 1 product of IR and microwave sensors, which are pre-processed by NOAA's National
168 Environmental Satellite, Data, and Information Service (NESDIS). For a complete list of the
169 thermal IR sensors, see Table 1 of Wei et al. (2021).

170 For AER, aerosol transmittance effects can be constrained in CRTM by ingesting three-
171 dimensional aerosol mixing ratios into GDAS. CRTM contains look-up tables for aerosol optical
172 properties—absorption coefficient, single scattering albedo, and asymmetric factor—to compute

173 the aerosol affected radiances (Lu et al. 2021). The optical properties are based on the Optical
174 Properties of Atmospheric Composition (OPAC) software package (Hess et al. 1998).

175 The aerosol mixing ratios are provided by the NEMS GFS Aerosol Component model
176 (NGAC, v2) (Fig. 1: gold), which is based on GOCART (Colarco et al. 2010). NGAC simulates
177 the emission, mixing, transport and removal (wet and dry) for 15 externally mixed aerosols,
178 including dust, sea salt, sulfate, organic carbon, and black carbon. (Lu et al. 2016; Wang et al.,
179 2018). The NGAC forecasts are used to predict the aerosols mixing ratios during the analysis
180 window of each cycle. Like the meteorological fields, the aerosol mixing ratios are interpolated
181 to the observations in space and time using the First Guess at Appropriate Time (FGAT) (Lorenc
182 and Rawlins 2005). Figure 2 shows the NGAC forecasts total AOD (all aerosols at 550nm)
183 averaged over August 1-28th, 2017. The AOD peaks over the Western Sahara, near the coast of
184 West Africa, and in the Bodéléle Depression, within the interior of the continent, which are
185 consistent with source regions over summertime in North Africa (Engelstader and Washington,
186 2007). The AOD, however, overestimates the hotspots by ~25% when compared to the summer
187 AOD climatology from the Modern-Era Retrospective analysis for Research and applications
188 (MERRA, v2) (Randles et al. 2016). Nonetheless, the use of NGAC does not affect our
189 qualitative interpretation of the aerosol-affected radiances on the analyses and forecasts.

190 We also conducted short-range forecasts in each experiments' fully cycled system. To do
191 this, the forecast model within GFS is used to run 120-hr weather forecasts at T670 (~30km)
192 resolution, which are initialized on 00 UTC of each day (Fig. 1: green). The forecast model does
193 account for aerosol radiative effects using prescribed monthly aerosol climatologies from OPAC
194 (Hess et al. 1998). But for both experiments, we use the *same* configuration in the forecast

195 model, which means that changes to the forecasts arise solely by the model's response to the
196 analysis differences, rather than the physics driving the forecast model.

197 To demonstrate the aerosol impact on the IR radiances, Fig. 3 shows a timeseries of each
198 experiment's observation-minus-forecast (OMF) BT for an IR channel (12.93 μm) from the
199 Infrared Atmospheric Sounding Interferometer (IASI); the channel and sensor are representative
200 for other IR window channels and thermal IR sensors, respectively. For both experiments, the
201 OMFs, which are averaged over North Africa and the East Atlantic, have a similar root-mean-
202 square (RMS) (Fig. 3a) and negative, or cold, bias (Fig. 3b) during the period of interest. But for
203 the cold bias, the AER run (red) is slightly more positive than the CTL run (blue). This
204 difference is due to the incorporation of aerosol transmittance effects on the forecast (simulated)
205 BT (via scattering), which in turn reduces the cold bias in the OMFs. The average impacts are
206 small ($\sim 1.7\text{K}$) over the region, but the bias differences can be substantial (up to $\sim 10\text{K}$) in
207 localized regions during strong Saharan dust events (Sokolik et al. 2001). When the aerosol-
208 affected OMFs are assimilated, this produces warmer analyzed temperatures at low-levels in the
209 atmosphere (Weaver et al. 2003; Kim et al. 2018; Wei et al. 2021).

210 *2.2 Wave tracking*

211 To identify the synoptic wave patterns during the period of interest, we used an objective
212 tracking algorithm similar to that in Brammer and Thorncroft (2015). Briefly, the tracking
213 algorithm involves analyzing mass-weighted centers of vorticity at multiple levels (i.e., curvature
214 vorticity at 850, 700, and 500 hPa; relative vorticity at 850 and 700 hPa). The wave center is then
215 determined from a weighted average of the centers within a specified radius (500 km). For each
216 experiment, the wave centers were extracted using the 6-hourly analysis fields, which identified
217 several systems that traversed North Africa and the East Atlantic. The tracking included waves

218 that later developed hurricanes, which we focus on in this study given their long lifetimes and
219 downstream implications.

220 For our time period of interest, two hurricanes developed from AEWs: Gert (2017) and
221 Harvey (2017). Figure 4 shows the objective track locations for the AEWs that developed
222 Hurricane Gert and Harvey in the CTL run over North Africa and the East Atlantic. For Gert
223 (solid line), the storm originates over Northeast Africa, at $5 - 10^{\circ}\text{N}$, on July 31st and moves
224 northwestward over North Africa and reaches the East Atlantic on August 4th. In contrast,
225 Harvey (dotted line) originates from two circulations over North Africa, at $25 - 29^{\circ}\text{N}$ and $8 -$
226 12°N , that develop on August 8th and merge into one circulation near the coast, on August 12th;
227 the storm then moves west/southwest over the East Atlantic. Both waves then developed
228 hurricanes while over the western portion of the Atlantic Ocean.

229 Comparison of the track locations for CTL and AER show little difference in the storm
230 positions during their evolution (not shown). After the initial development, the track locations
231 among the two cases are less than 250 km. Given the wavelength of the AEWs span 2000 – 5000
232 km (Burpee 1974), the aerosol-aware assimilation does not appear to have a significant influence
233 on the wave tracks. Therefore, we use track locations from CTL when investigating the storm
234 structures in the analyses and forecasts for both cases.

235 **3. Results**

236 *3.1 Analysis Differences: Time-average fields*

237 Before investigating the AEW cases shown in Fig. 4, we first examine the aerosol
238 impacts on the time-averaged background temperature, background zonal wind, and AEW
239 meridional wind variances.

240 Figure 5 shows cross-sections of the time-averaged background temperature and zonal
241 wind for CTL (contours) and the AER – CTL difference (colors) averaged over August 1st-28th,
242 2017. Consider first the CTL run. The experiment captures the main summertime circulation
243 features over the region. For temperatures, the warmest air is positioned near the surface over the
244 Saharan Desert (Fig 5a: 20°N-30°N). This warming sets up a strong meridional temperature
245 gradient that extends vertically up to ~650 hPa and horizontally across the Sahel and over the
246 East Atlantic (Fig. 5b: 30°W-20°E). For the zonal wind, there is a well-defined AEJ at 650 hPa
247 (Fig. 5c: 15°N) that extends across North Africa and the East Atlantic (Fig. 5d: 20°W – 15°E,
248 10°N – 15°N) and low-level westerlies (800-1000 hPa) that are associated with the West African
249 Monsoon (WAM) flow (Fig 5c: 8°N-18°N).

250 The AER – CTL differences in Fig. 5 indicate how the aerosol-affected radiances impact
251 the time-averaged background fields. For temperature, the aerosol impacts warm the Sahara and
252 Sahel in the boundary layer by ~0.5 K (reddish colors in Fig. 5a: 10°N – 30°N, 1000 hPa – 650
253 hPa) and cool the marine boundary layer below the SAL by ~0.5 K (blueish colors in Fig. 5b:
254 15°N – 25°W, 15°N – 30°N). These temperature changes are qualitatively consistent with
255 enhanced aerosol heating in the boundary layer over the continent and in the SAL offshore. Over
256 land, the heating peaks at 800 hPa in the Sahel and the southern Saharan Desert (Fig 5a: 15°N -
257 25°N). The position of the heating means that the aerosol-aware assimilation (i) increases lapse
258 rates (or reduced static stability) at low levels in the Sahel and southern Sahara (15°N – 25°N
259 1000 – 800 hPa) and (ii) enhances the meridional temperature gradient in the Sahel (Fig 5a:
260 12°N – 20°N, 1000-600 hPa; Fig 5b: 10°W-10°E, 12°N-20°N).

261 The AER – CTL differences in temperature support the changes to background zonal
262 wind via adjustments to the thermal wind. For example, along the enhanced meridional

263 temperature gradient (12°N - 20°N), AER accelerates the AEJ by ~ 0.5 m/s (blueish colors in Fig.
264 5c: $10^{\circ}\text{N} - 15^{\circ}\text{N}$, 700 – 600 hPa, and Fig. 5d: $20^{\circ}\text{E} - 30^{\circ}\text{W}$, $10 - 15^{\circ}\text{N}$), and accelerates the
265 westerly flow of the WAM by about ~ 1.0 m/s (reddish colors in Fig. 5c: $12^{\circ}\text{N} - 19^{\circ}\text{N}$, 1000 –
266 850 hPa). Away from these features, the structural changes to the zonal wind are more difficult
267 to interpret. But assessment of shear difference plots (not shown) show that the aerosol-aware
268 assimilation: (i) increases the vertical shear below the AEJ ($15^{\circ}\text{N} - 22^{\circ}\text{N}$, 900 – 700 hPa) and
269 (ii) decreases the horizontal shear on the flanks of the AEJ axis ($8^{\circ}\text{N} - 18^{\circ}\text{N}$, 800 – 600 hPa).

270 Figure 6 shows a vertical cross-section of the time-averaged, 2-6 day filtered meridional
271 wind variance, a proxy used to assess AEW amplitudes (Reed et al. 1988; Pytharilous and
272 Thorncroft 1999). The filtered meridional wind variances capture the two AEW tracks over the
273 interior of North Africa (contours show the CTL run). For both experiments, the wave structures
274 peak at levels consistent with AEWs examined in previous studies (southern: $8^{\circ}\text{N} - 13^{\circ}\text{N}$, 700 –
275 600; northern: $18^{\circ}\text{N} - 22^{\circ}\text{N}$, 950 – 800 hPa). But the AER – CTL differences (colors) show that
276 for the AER run, the meridional wind variances increase by $\sim 15\%$ in the northern circulation and
277 decrease by $\sim 10\%$ in the southern circulation. Note that the AER run also increases the wind
278 variances near the AEJ core by $\sim 25\%$ (15°N , 600 hPa), but this increase does not change the
279 peak location of the southern circulation.

280 The differences in the AEW meridional wind variances shown in Fig. 6 are, in part, due
281 to changes to the background fields, which can be explained by the local wave energetics
282 (Norquist et al. 1977; Hseih and Cook 2005; Bercos-Hickey et al. 2020). In absent of diabatic
283 processes, the AEW's southern structure extracts energy from the background via barotropic
284 conversions, which are proportional to the horizontal shear of the AEJ, while the northern
285 structure extracts energy via baroclinic energy conversions, which are inversely proportional to

286 the static stability (Thorncroft and Hoskins 1994; Paradis et al. 1995; Thorncroft 1995). This
287 means that for AER, the changes to the background zonal wind and temperature (i) reduce wind
288 variances in the southern circulation via decreased horizontal shear on the equatorward side of
289 the AEJ (barotropic) and (ii) increase wind variances in the northern circulation via reduced
290 static stability below the AEJ (baroclinic).

291 The qualitative explanation of how aerosol-affected radiances impact the waves via the
292 background fields aligns with the first of two pathways in which dust can affect AEWs
293 mentioned in the introduction. For AER, the aerosol-aware assimilation captures dust radiative
294 effects that operate on the analyzed background temperature, AEJ, and thus the AEW wind
295 variances. But it's worth mentioning that dust radiative effects are coupled to the forecast model
296 (i.e., from the OPAC aerosol climatology), which also operate on the analysis fields via the first-
297 guess meteorological fields. Thus in AER, changes to the time-averaged fields in Figs. 5 and 6
298 are due to the time-averaged NGAC aerosols in the assimilation system modifying existing
299 radiative effects imposed by the OPAC aerosol climatology in the forecast model. To investigate
300 the impact of episodic dust plumes in the assimilation, we turn next to our AEW cases.

301 *3.2 Analysis Differences: AEW cases*

302 Figure 7 compares the structure of the AEW that developed Gert for CTL and AER. The
303 AEW crosses Africa and the East Atlantic from July 31st to August 4th. During these times, the
304 wave remains south of the AEJ and is thus largely away from the dust aerosols. But despite this
305 separation, the aerosol-aware assimilation affects the evolution of the wave structure (Fig 7a, 7c:
306 colors surrounding the X's). For example, on Aug 2nd, the AER run decreases the wave, which is
307 an open trough (Fig 7a: blueish colors surrounding the X). The vertical structure also shows that
308 the vorticity for AER (red) is ~10% less than the for CTL (blue) from 600 – 800 hPa (Fig. 7b).

309 On Aug 4th, the wave intensifies as it moves offshore, forming a closed streamline circulation
310 (Fig. 7c). But similar to the onshore wave, the aerosol impacts on the vertical structures continue
311 to reduce the cyclonic vorticity within the storm center by ~10% (Fig. 7d).

312 Figure 8 compares the structure of the AEW that developed Harvey for CTL and AER.
313 The AEW develops as two circulations over East Africa on August 8th and travels west. On
314 August 9th the land-based AEW is broad in structure and covers a large portion of the continent
315 (Fig. 8a). For AER, there are strong changes within both circulation centers, which include
316 increases in the vorticity around the northern circulation structure (reddish colors at 18°N) and
317 decreases in the southern circulation (blueish colors at 14°N). The vertical structures show that
318 vorticity for the northern circulation is, on average, ~20 – 35% larger from 600-850 hPa (Figs.
319 8b: cf. solid blue and solid red), while the southern circulation is ~20 – 35% smaller from 750-
320 850 hPa (Figs. 8b: cf. dotted blue and dotted red). On August 12th, the two circulations merge
321 into a single wave offshore. Compared to the land-based AEW, the amplitudes of the combined
322 wave are weak and its vertical structure changes little with height (Fig 8c, 8d). Consequently, the
323 aerosol impacts are reduced, affecting the vorticity by ~5-15% from 1000-500 hPa (Fig. 8d).

324 Over Africa, the aerosol impacts on the AEWs for Gert and Harvey were consistent with
325 the time-averaged AEW meridional wind variances in Fig. 6, but the impacts were stronger for
326 Harvey. The story is different offshore: the impacts remain moderate for Gert but weaken for
327 Harvey; the latter may be due to the merging of the circulations and the positioning of the
328 aerosols. Therefore, we focus on land-based AEWs and further investigate the aerosol impacts.

329 To understand how the aerosol-aware assimilation impacts our AEW cases, it is
330 informative to examine the episodic dust plumes and radiance observations as the waves crosses
331 West Africa. Thus, Fig. 9 shows a snapshot of the NGAC AOD (brown contours) for times when

332 the AEW for Gert (a) and Harvey (b) are over Africa; the X's mark the position of the circulation
333 centers. Overlaying the AOD are observations from the IASI sensor at the same time; shown are
334 the AER – CTL differences in the BT at 12.93 μ m (circles), the same sensor and channel shown
335 in Fig 3. For Gert, the BT differences surrounding the wave center are negative. This indicates
336 that near the wave center, the BTs are cooler in the AER run (Fig. 9a), but the values are small
337 (light blue circles). In contrast, for Harvey, the negative values are large near the northern
338 circulation (dark blue circles), which is also immersed in a dust plume with AODs over 1.0 (Fig.
339 9b).

340 When aerosol-affected radiances are assimilated, warmer analyzed temperatures are
341 produced at low-levels over North Africa and the East Atlantic (Kim et al. 2018; Wei et al.
342 2021). For the AEW that developed Gert, the warming over Africa is similar to the time-
343 averaged AER-CTL background temperatures shown in Figs. 5a and 5b. For the AEW that
344 developed Harvey in AER, however, the temperatures over the wave's northern circulation (18-
345 22°N) warms as much as 1.5 K at mid-levels, 900-600 hPa, which is double the average. The
346 implications of this additional warming on the AEW vorticity is explained below.

347 Grogan and Thorncroft (2019) showed through energetic arguments that the heating from
348 an episodic dust signal that interacts with the AEW's northern circulation generates eddy
349 available potential energy ($APE \sim T'^2$). Previous idealized studies have also shown that dust-
350 induced eddy APE amplifies the northern structure of AEWs (Grogan et al. 2016, 2019; Nathan
351 et al. 2017; Bercos-Hickey et al. 2017). For the Harvey case in the AER run, the scenario is the
352 same as in Grogan and Thorncroft (2019), but the aerosol-affected radiances capture the heating
353 from the dust plume, rather than the forecast model, which in turn drives the amplified vorticity
354 in the AEW's northern circulation.

355 The qualitative explanation of how aerosol-affected radiances impact the AEW that
356 developed Harvey via the episodic dust field aligns with the second pathway in which dust can
357 affect AEWs mentioned in the introduction. Thus, the combined effects may help to explain why
358 the aerosol impacts for the AEW with Harvey is stronger than the AEW with Gert.

359 *3.3 Forecast Differences: AEW cases*

360 To examine the impact of the aerosol-aware assimilation on the forecasts for our AEW
361 cases, we compare the Root-Mean-Square-Error (RMSE) in vorticity for CTL and AER; the
362 forecasts were verified against their respective analysis. Table 1 shows the RMSE relative
363 differences between AER and CTL for the 1000 – 500 hPa vorticity following the AEWs. To
364 compute the RMSE following the AEW at each forecast time, we use the CTL wave locations
365 shown in Section 2. For Gert, a 10° latitude by 10° longitude window is centered on the wave.
366 For Harvey, our window over North Africa has a fixed latitude of 5 – 25°N and a 15° longitude
367 range that is centered on the two circulations; over the Atlantic Ocean, a 10° latitude by 10°
368 longitude window is centered on the merged circulation.

369 Table 1 shows the AER run produces neutral improvement in the forecasting of the AEW
370 that developed Gert, as evidenced by the mixture of red and green values in the RMSE relative
371 differences. Inspection of the forecasts show that both AER and CTL underestimate the
372 intensification of the AEW when initialized onshore, on July 31st – Aug 2nd, and overestimate the
373 intensification when initialized offshore, on Aug 3rd. As a result, there were several instances
374 where the RMSE forecast differences did not produce statistically significant results (i.e., crossed
375 out values for Gert in Table 1).

376 In contrast to the AEW that developed Gert, Table 1 shows the AER run produces
377 statistically significant improvement in forecasting the AEW that developed Harvey. The largest

378 improvements are found on the forecasts initialized on August 10th and 11th, with the forecast on
379 August 10th showing reductions in RMSE on every forecast day (errors reduced by ~15-49%).
380 For the initialized times that we examine for Harvey (Aug 8th -11th), both the analyzed
381 amplitudes and AER – CTL vorticity differences were larger than Gert while onshore (cf. Figs. 6
382 and 8). Inspection of the forecasts reveal that the CTL run continues to suppress the wave
383 amplitudes downstream, while the AER run better maintains the intensity of the wave as the two
384 circulations merge over the East Atlantic and travel downstream.

385 In summary, the forecast error of the 1000-500 hPa averaged vorticity for the AEW that
386 developed Gert are similar among the two experiments, but dramatically reduced in AER for the
387 AEW that developed Harvey. This marked improvement with Harvey is likely associated with
388 the aerosol-aware assimilation capturing radiative effects of the large-scale Saharan dust plume
389 that interacted with the AEWs northern circulation. Therefore, ingesting mixing ratios of
390 episodic aerosols to constrain radiance calculations within the assimilation system can improve
391 forecasting the evolution of AEWs.

392 **4. Conclusions and Discussion**

393 In this study, we examined how incorporating time-varying aerosols into the assimilation
394 of satellite radiances affected the analyses and forecasts using GFS v14 and the corresponding
395 GDAS. In particular, we investigated the impacts of Saharan dust on the analyses and forecasts
396 of AEWs and their environment over North Africa and the East Atlantic during August 2017. To
397 do this, aerosol forecasts from the NGAC, v2 model were ingested into GDAS and constrained
398 to the radiance calculations to produce analysis fields (aerosol-aware) that were compared to a
399 control experiment that excluded aerosols (aerosol-blind). The analysis fields from both cases
400 were then used to forecast two AEW cases during our time period that were structurally different

401 over Africa, but later developed Hurricane Gert (2017) and Harvey (2017) over the Atlantic
402 Ocean.

403 Analysis differences showed that the aerosol-aware assimilation affected several fields
404 over North Africa and the East Atlantic. For example, the aerosols warmed the Saharan boundary
405 layer, accelerated the AEJ and the westerlies associated with the WAM, and modified AEW
406 meridional variances, with amplitudes increasing within the northern circulation and decreasing
407 in the southern circulation. The changes in the AEW meridional variances were also consistent
408 with the vorticity changes for the individual AEW cases examined.

409 The impact of the analysis differences on forecasting the AEW cases was also examined.
410 For the AEW that developed Gert, RMSE differences showed that the aerosol-aware experiment
411 produced neutral improvement to the vorticity field among the forecasts tracking the wave over
412 North Africa and the Atlantic. In contrast, the aerosol-aware experiment improved the vorticity
413 field in most forecasts for the AEW that developed Harvey; the largest reductions in RMSE
414 occurred when analysis differences in the AEW structures were largest.

415 In exploring the results, we showed qualitatively that the aerosol-aware experiment (via
416 NGAC aerosols) captured the two pathways involving dust radiative effects on the AEWs that
417 are mentioned in the introduction. For example, the aerosol-aware experiment modified the
418 analyzed background temperature and AEJ, which in turn modified the analyzed time-averaged
419 AEWs (the first pathway). Additionally, the aerosol-aware assimilation captured the enhanced
420 warming and vorticity associated with the formation of an episodic plume interacting the
421 northern circulation of the AEW that developed Harvey (second pathway). This response is
422 similar for dust-coupled AEWs (Grogan and Thorncroft 2019). In contrast, this effect was absent

423 for the AEW the developed Gert, which did not have a northern circulation nor interact with a
424 dust plume.

425 The improvement on forecasting the AEW that developed Harvey suggests the
426 importance of the aerosol-aware assimilation capturing dust radiative effects on AEWs involving
427 episodic dust plumes. The AEW that developed Gert, however, was influenced by the radiative
428 effects involving the time-averaged background fields, which were captured by the forecast
429 model (via OPAC) and the aerosol-aware assimilation (via NGAC), did not improve forecasting
430 the storm. Therefore, investigating more cases, both of which that interact with episodic dust
431 plumes and those that do not, would better determine the utility of our approach for forecasting
432 AEWs. Moreover, there are known variabilities in AEW activity (Brammer and Thorncroft
433 2017) and dust source regions over West Africa (Wagner et al. 2016) that should also be
434 examined. Nonetheless, forecast improvements such as those shown for the AEW that
435 developed Harvey are encouraging and could be critical for determining the timing and location
436 of tropical cyclogenesis that originate from developing AEWs.

437 Aerosol radiative effects can be incorporated into the NWP system through the forecast
438 model and through the assimilation system. Though few studies focus on the assimilation
439 approach, such as Kim et al. (2018) and Wei et al. (2021), this study has demonstrated the
440 importance of incorporating time-varying, episodic aerosols into the satellite radiance
441 calculations to capture dust radiative effects on the analyzed AEWs. More work, however, is
442 needed to better understand how to optimize the aerosol-aware assimilation, such as adjusting the
443 bias-correction and quality-control procedures (Wei et al. 2021). Moreover, future work should
444 investigate how much complexity is needed to represent aerosol processes adequately and
445 accurately, and thus effectively account for aerosol effects within the NWP system.

446 **Data availability**

447 Analyses and forecasts from the AER and CTL runs can be provided upon request to the
448 first author of the paper.

449 **Author contributions**

450 DG and SL developed the ideas for the study. SW and SC conducted the numerical
451 experiments. DG, CL, and SW analyzed and interpreted the results. DG prepared the paper. DG,
452 CL and SW reviewed the paper.

453 **Competing interests**

454 The authors declare that they have no conflicts of interest.

455 **Acknowledgements**

456 The work presented here is supported by NOAA NWS NGGPS R2O (Award number
457 #NA15NWS468008). The NWS project is a collaborative effort from the University at Albany
458 (Cheng-Hsuan Lu, Shih-Wei Wei, Sheng-Po Chen, and Dustin Grogan), NCEP/EMC (Robert
459 Grumbine, Andrew Collard, Jun Wang, Partha Bhattacharjee, Bert Katz, Xu Li), and
460 NESDIS/STAR (Quanhua Liu, Zhu Tong). The GDAS experiments were conducted at the
461 University of Wisconsin-Madison Space Science and Engineering Center's Satellite Simulations
462 and Data Assimilation Studies computer, or S4, cluster.

463 **References**

- 464 Bercos-Hickey, E., Nathan, T.R., and Chen, S.-H.: Saharan dust and the African easterly jet–
465 African easterly wave system: structure, location and energetics. *Q. J. R. Meteorol. Soc.*,
466 143, 2797-2808, <https://doi.org/10.1002/qj.3128>, 2017.
- 467 Bercos-Hickey, E., Nathan, T.R., and Chen, S.-H.: On the Relationship between the African
468 Easterly Jet, Saharan Mineral Dust Aerosols, and West African Precipitation. *J. Clim.*, 143,
469 3533-3546, <https://doi.org/10.1175/JCLI-D-18-0661.1>, 2020
- 470 Benedetti A., and Coauthors: Status and future of numerical atmospheric aerosol prediction with
471 a focus on data requirements. *Atmos. Chem. Phys.*, 18, 10615-10643,
472 <https://doi.org/10.5194/acp-18-10615-2018>, 2018.
- 473 Berry G.J., and Thorncroft C.D.: Case study of an intense African easterly wave. *Mon. Wea. Rev.*
474 123: 752-766, <https://doi.org/10.1175/MWR2884.1>, 2005
- 475 Brammer, A., and Thorncroft, C.D.: Variability and evolution of African easterly wave structures
476 and their relationship with tropical cyclogenesis over the eastern Atlantic. *Mon. Wea. Rev.*
477 143, 4975-4995, <https://doi.org/10.1175/MWR-D-15-0106.1>, 2015.
- 478 Brammar A., and Thorncroft, C.D.: Spatial and temporal variability of the three-dimensional
479 flow around African easterly waves. *Mon. Wea. Rev.*, 145, 2879-2897,
480 <https://doi.org/10.1175/MWR-D-16-0454.1>, 2017.
- 481 Bozzo, A., Remy, S., Benedetti, A., Fleming, J., Betchold, P., Rodwell, M.J., and Morcrette, J.-
482 J.: Implementation of a CAMS-based aerosol climatology in the IFS. ECMWF Technical
483 Memorandum, 801, Available at: [https://www.ecmwf.int/en/elibrary/17771-radiation-](https://www.ecmwf.int/en/elibrary/17771-radiation-numerical-weather-prediction)
484 [numerical-weather-prediction](https://www.ecmwf.int/en/elibrary/17771-radiation-numerical-weather-prediction) (last access: 1 Feb 2021), 2017.
- 485 Burpee, R.W.: The origin and structure of easterly waves in the lower troposphere of North
486 Africa. *J. Atmos. Sci.*, 29, 77-90, [https://doi.org/10.1175/1520-](https://doi.org/10.1175/1520-0469(1972)029<0077:TOASOE>2.0.CO;2)
487 [0469\(1972\)029<0077:TOASOE>2.0.CO;2](https://doi.org/10.1175/1520-0469(1972)029<0077:TOASOE>2.0.CO;2), 1972.
- 488 Burpee, R.W.: Characteristics of North African Easterly Waves During the Summers of 1968
489 and 1969. *J. Atmos. Sci.*, 31, 1556-1570, [https://doi.org/10.1175/1520-](https://doi.org/10.1175/1520-0469(1974)031<1556:CONAEW>2.0.CO;2)
490 [0469\(1974\)031<1556:CONAEW>2.0.CO;2](https://doi.org/10.1175/1520-0469(1974)031<1556:CONAEW>2.0.CO;2), 1974.
- 491 Carlson, T. N.: Some Remarks on African Disturbances and their Progress over the Tropical
492 Atlantic. *Mon. Wea. Rev.*, 97, No. 10, 716-726, [https://doi.org/10.1175/1520-](https://doi.org/10.1175/1520-0493(1969)097<0716:SROADA>2.3.CO;2)
493 [0493\(1969\)097<0716:SROADA>2.3.CO;2](https://doi.org/10.1175/1520-0493(1969)097<0716:SROADA>2.3.CO;2), 1969.
- 494 Chen, S.-H., Liu, Y.-C., Nathan, T.R., Davis, C., Torn, R., Sowa N., Cheng, C.-T., and Chen, J.-
495 P.: Modeling the effects of dust-radiative forcing on the movement of Hurricane Helene
496 (2006). *Q. J. R. Meteorol. Soc.*, <https://doi.org/10.1002/qj.2542>, 2015.
- 497 Colarco, P., da Silva A., Chin M., Diehl T.: Online simulations of global aerosol distributions in
498 the NASA GEOS-4 model and comparisons to satellite and ground-based aerosol optical
499 depth. *J. Geophys. Res.* 115: D14207. <https://doi.org/10.1029/2009JD012820>, 2010
- 500 Cowie, S.M., Knippertz, P., and Marsham, J.H.: A climatology of dust emission events from
501 northern Africa using long-term surface observations. *Atmos. Chem. Phys.*, 14, 8579-8597,
502 <https://doi.org/10.5194/acp-14-8579-2014>, 2014.

- 503 Cuesta, J., Marsham J.H., Parker D.H., Flamant C.: Dynamical mechanisms controlling the
504 vertical redistribution of dust and the thermodynamic structure of the West Saharan
505 atmospheric boundary layer during summer. *Atmos. Sci. Lett.* 10: 34-42.
506 <https://doi.org/10.1002/asl.207>, 2009.
- 507 Engelstaedter, S., and Washington R.: Atmospheric controls on the annual cycle of North African
508 dust. *J. Geophys. Res.-Atmos.* 112: D03103, <https://doi.org/10.1029/2006JD007195>, 2007.
- 509 Grogan, D.F.P., Nathan, T.R., and Chen, S.-H.: Effect of Saharan dust on the linear dynamics of
510 African easterly waves. *J. Atmos. Sci.* 73, 891-911, <https://doi.org/10.1175/JAS-D-15-0143.1>, 2016.
- 512 Grogan, D.F.P., Nathan, T.R., and Chen, S.-H.: Saharan dust and the nonlinear evolution of the
513 African easterly jet–African easterly wave system. *J. Atmos. Sci.* 74, 24-47,
514 <https://doi.org/10.1175/JAS-D-16-0118.1>, 2017.
- 515 Grogan, D.F.P. and Thorncroft, C.D.: The characteristics of African easterly waves coupled to
516 Saharan mineral dust aerosols. *Q. J. R. Meteorol. Soc.* 2019, 1–17,
517 <https://doi.org/10.1002/qj.3483>, 2019.
- 518 Grogan, D.F.P., Nathan, T.R., and Chen, S.-H.: Structural Changes in the African Easterly Jet
519 and Its Role in Mediating the Effects of Saharan Dust on the Linear Dynamics of African
520 Easterly Waves. *J. Atmos. Sci.* 76, 3359-3365, <https://doi.org/10.1175/JAS-D-19-0104.1>,
521 2019.
- 522 Han, Y., van Deist, P., Liu, Q., Weng, F., Yan, B., Treason, R., and Derber, J.: JCSDA
523 community radiative transfer model (CRTM): Version 1. NOAA Technical Report
524 NESDIS 122. Available at
525 https://repository.library.noaa.gov/view/noaa/1157/noaa_1157_DS1.pdf (last access: 1 Feb
526 2021), 2006.
- 527 Hess, M.P., Koepke, P., and Shult, I.: Optical properties of aerosol and clouds: The software
528 package OPAC. *Bull. Amer Meteor. Soc.*, 79, 831-844, [https://doi.org/10.1175/1520-0477\(1998\)079<0831:OPOAAC>2.0.CO;2](https://doi.org/10.1175/1520-0477(1998)079<0831:OPOAAC>2.0.CO;2), 1998.
- 530 Hsieh, J.-S., and Cook, K.H.: Generation of African easterly wave disturbances: relationship to
531 the African easterly jet. *Mon. Wea. Rev.*, 133, 1311-1327,
532 <https://doi.org/10.1175/MWR2916.1>, 2005.
- 533 Jones, C., Mahowald, N., Luo, C. The role of easterly waves on African desert dust transport. *J.*
534 *Clim.* 16: 3617-3628. [https://doi.org/10.1175/1520-0442\(2003\)016<3617:TROEWO>2.0.CO;2](https://doi.org/10.1175/1520-0442(2003)016<3617:TROEWO>2.0.CO;2), 2003.
- 536 Jones, C., Mahowald, N., and Luo, C.: Observational evidence of African desert dust
537 intensification of easterly waves. *Geophys. Res. Lett.*, 31, L17208,
538 <https://doi.org/10.1029/2004GL020107>, 2004.
- 539 Jury, M.R. and Santiago, M.J.: Composite analysis of dust impacts on African easterly waves in
540 the Moderate Resolution Imaging Spectrometer era. *J. Geophys. Res.*, 115, D16213,
541 <https://doi.org/10.1029/2009JD013612>, 2010.
- 542 Karyampudi, V.M., and Coauthors: Validation of the Saharan Dust Plume Conceptual Model
543 Using Lidar, Meteosat, and ECMWF Data. *Bull. Amer. Meteor. Soc.*, 1045-1076,

544 [https://doi.org/10.1175/1520-0477\(1999\)080<1045:VOTSDP>2.0.CO;2](https://doi.org/10.1175/1520-0477(1999)080<1045:VOTSDP>2.0.CO;2), 1999.

545 Kiladis, G.N., Thorncroft, C.D., and Hall, N.M.J.: Three-Dimensional Structure and Dynamics
546 of African Easterly Waves. Part I: observations. *J. Atmos. Sci.* 63, 2212-2230,
547 <https://doi.org/10.1175/JAS3741.1>, 2006.

548 Kim, J., Akella, S., da Silva, A.M., Todling, R., and McCarty, W.: Preliminary evaluation of
549 influence of aerosols on the simulation of brightness temperature in NASA's Goddard
550 Earth Observing System Atmospheric Data Assimilation System. Technical Report Series
551 on Global Modeling and Data Assimilation, 49. Available at
552 <https://ntrs.nasa.gov/api/citations/20180001946/downloads/20180001946.pdf> (last access:
553 1 Feb 2021), 2018.

554 Knippertz P, and Todd, M.C.: The central west Saharan dust hot spot and its relation to African
555 easterly waves and extratropical disturbances. *Geophys. Res. Lett.* 115.
556 <https://doi.org/10.1029/2009D012819>, 2010

557 Knippertz, P., and Todd, M.: Mineral dust aerosols over the Sahara: Meteorological controls on
558 emission and transport and implications for modeling. *Rev. Geophys.*, 50, RG1007,
559 <https://doi.org/10.1029/2011RG000362>, 2012.

560 Lorenc, A.C., and Rawlins, F.: Why Does 4D-Var Beat 3D-Var? *Q. J. R. Meteorol. Soc.* 2005,
561 131, 3247–3257, <https://doi.org/10.1256/qj.05.85>, 2005.

562 Lu, C.-H., and Coauthors: The implementation of NEMS GFS Aerosol Component (NGAC)
563 Version 1.0 for global dust forecasting at NOAA/NCEP. *Geosci. Model Dev.*, 9, 1906-
564 1919, <https://doi.org/10.5194/gmd-9-1905-2016>, 2016.

565 Lu, C.-H., and Coauthors: The Aerosol Module in the Community Radiative Transfer Model
566 (v2.2 and v2.3): accounting for aerosol transmittance effects on the radiance observation
567 operator, et al. *Geosci. Model Dev.*, under review, <https://doi.org/10.5194/gmd-2021-145>,
568 2021.

569 Hou, Y.-T., Moorhi, S., and Campana, K.: Parameterization of solar radiation transfer in the
570 NCEP models. NCEP Office Note 441. Available at
571 https://repository.library.noaa.gov/view/noaa/23085/noaa_23085_DS1.pdf (last access: 1
572 Feb 2021), 2002.

573 Mulcahey, J.-P., Walters, D.N., Bellouin, N., and Milton, S.F.: Impacts of increasing the aerosol
574 complexity in the Met Office global numerical weather prediction model. *Atmos. Chem.*
575 *Phys.*, 14, 4749–4778, <https://doi.org/10.5194/acp-14-4749-2014>, 2014.

576 Nathan, T.R., Grogan, D.F.P., and Chen, S.-H.: Subcritical destabilization of African easterly
577 waves by Saharan mineral dust. *J. Atmos. Sci.* 74, 1039-1055, [https://doi.org/10.1175/JAS-](https://doi.org/10.1175/JAS-D-16-0247.1)
578 [D-16-0247.1](https://doi.org/10.1175/JAS-D-16-0247.1), 2017.

579 Nathan, T.R., Grogan, D.F.P. and Chen. S.-H.: Saharan dust transport during the incipient
580 growth phase of African easterly waves. *Geosciences*, 9, 388,
581 <https://doi.org/10.3390/geosciences9090388>, 2019.

582 Norquist, D.C., Recker, E.R., and Reed, R.J.: The Energetics of African Wave Disturbances as
583 observed During Phase III of GATE. *Mon. Wea. Rev.*, 105, 334–342,
584 [https://doi.org/10.1175/1520-0493\(1977\)105<0334:TEOAWD>2.0.CO;2](https://doi.org/10.1175/1520-0493(1977)105<0334:TEOAWD>2.0.CO;2), 1977.

585 Paradis, D., Lafore, J.-P., Redelsperger, J.-L., and Balaji, V.: African easterly waves and
586 convection. Part I: linear simulations. *J. Atmos. Sci.*, 52, 1657-1679,
587 [https://doi.org/10.1175/1520-0469\(1995\)052<1657:AEWACP>2.0.CO;2](https://doi.org/10.1175/1520-0469(1995)052<1657:AEWACP>2.0.CO;2), 1995.

588 Pérez, C., Nickovic, S., Pejanovic, G., Baldasano, J.M., and Özsoy, E.: Interactive dust-radiation
589 modeling: A step to improve weather forecasts. *J. Geophys. Res. Lett.*, 111, D16206,
590 <https://doi.org/10.1029/2005JD006717>, 2006.

591 Pytharoulis, I., and Thorncroft, C.D.: The low-level structure of African easterly waves in 1995.
592 *Mon. Wea. Rev.*, 127, 2266–2280, [https://doi.org/10.1175/1520-0493\(1999\)127<2266:TLLSOA>2.0.CO;2](https://doi.org/10.1175/1520-0493(1999)127<2266:TLLSOA>2.0.CO;2), 1999.

594 Randles, C. A., and Coauthors: The MERRA-2 Aerosol Assimilation. NASA TM-2016-104606,
595 Vol. 45, NASA Global Modeling and Assimilation Office, 132 pp,
596 <https://gmao.gsfc.nasa.gov/pubs/docs/Randles887.pdf>, 2016.

597 Reed, R. J., Klinker, E., and Hollingsworth, A.: The structure and characteristics of African
598 easterly wave disturbances as determined from the ECMWF operational analysis/forecast
599 system. *Meteorol. Atmos. Phys.*, 38, 22-33, <https://doi.org/10.1007/BF01029944>, 1988.

600 Reale, O., Lau, K.M., Kim, K.-Y., and Brin, E.: Atlantic Tropical Cyclogenetic Processes during
601 SOP-3 NAMMA in the GEOS-5 Global Data Assimilation and Forecast System. *J. Atmos.*
602 *Sci.*, 66, 3563–3578, <https://doi.org/10.1175/2009JAS3123.1>, 2009.

603 Reale, O., and Lau, K.M.: Impact of an interactive aerosol on the African easterly jet in the
604 NASA GOES-5 global forecasting system. *Wea. Forecasting*, 26, 504-519,
605 <https://doi.org/10.1175/WAF-D-10-05025.1>, 2011.

606 Reale, O., Lau, K.M., da Silva, A.M., and Matsui, T.: Impact of assimilated and interactive
607 aerosol on tropical cyclogenesis. *Geophys. Res. Lett.*, 41, 3282–3288,
608 <https://doi.org/10.1002/2014GL059918>, 2014.

609 Ross, R. S., and Krishnamurti, T.N.: Low-level African easterly wave activity and its relation to
610 Atlantic tropical cyclogenesis in 2001. *Mon. Wea. Rev.*, 135, 3950–3964,
611 <https://doi.org/10.1175/2007MWR1996.1>, 2007.

612 Schwendike, J., and Jones, S.C.: Convection in an African Easterly Wave over West Africa and
613 the eastern Atlantic: A model case study of Helene (2006). *Q. J. R. Meteorol. Soc.*, 135,
614 364-396, <https://doi.org/10.1002/qj.566>, 2010.

615 Sokolik, I.: The spectral radiative signature of wind-blown mineral dust: Implications for remote
616 sensing in the thermal IR region. *Geophys. Res. Lett.*, 29, NO. 24, 2154,
617 <https://doi.org/10.1029/2002GL015910>, 2002.

618 Thorncroft, C.D., and Hoskins, B.J.: An idealized study of African easterly waves. I: Linear
619 theory. *Q. J. R. Meteorol. Soc.*, 120, 953-982, <https://doi.org/10.1002/qj.49712051809>,
620 1994.

621 Thorncroft, C.D.: An idealized study of African easterly waves. III: More realistic basic states. *Q.*
622 *J. Roy. Meteorol. Soc.* 121, 1589–1614. <https://doi.org/10.1002/qj.49712152706>, 1995.

623 Tegen, I., and Fung I.: Modeling of mineral dust in the atmosphere: Sources, transport, and
624 optical thickness. *J. Geophys. Res.* 99, 22897-22914. <https://doi.org/10.1029/94JD01928>,
625 1994.

626 Wagner, R., Schepanski, K., Heinold, B., and Tegen, I.: Interannual variability in the Saharan
627 dust source activation—toward understanding the differences between 2007 and 2008. *J.*
628 *Geophys Res. -Atmos* 121, 4538–4562. <https://doi.org/10.1002/2015JD024302>, 2017.

629 Wang, J., and Coauthors: The implementation of NEMS GFS Aerosol Component (NGAC)
630 Version 2.0 for global multispecies forecasting at NOAA/NCEP— Part 1: Model
631 descriptions, *Geosci. Model Dev.*, 11, 2315–2332, [https://doi.org/10.5194/gmd-11-2315-](https://doi.org/10.5194/gmd-11-2315-2018)
632 [2018](https://doi.org/10.5194/gmd-11-2315-2018), 2018.

633 Weaver, C.J., Joiner, J., and Ginoux, P.: Mineral aerosol contamination of TIROS Operational
634 Vertical Sounder (TOVS) temperature and moisture retrievals. *J. Geophys. Res.* 2003, 108.
635 <https://doi.org/10.1029/2002JD002571>, 2003.

636 Webb, N.P., and Strong, C.L.: Soil erodibility dynamics and its representation for wind erosion
637 and dust emission models. *Aeolian Res.* 3, 165-179,
638 <https://doi.org/10.1016/j.aeolia.2011.03.002>, 2011.

639 Westphal, D.L., Toon O.B., and Carlson, T.N.: A case study of mobilization and transport of
640 Saharan dust. *J. Atmos. Sci.* 45, 2145-2175, [https://doi.org/10.1175/1520-](https://doi.org/10.1175/1520-0469(1988)045<2145:ACSOMA>2.0.CO;2)
641 [0469\(1988\)045<2145:ACSOMA>2.0.CO;2](https://doi.org/10.1175/1520-0469(1988)045<2145:ACSOMA>2.0.CO;2), 1988.

642 Wei, S.-W., Collard, A., Grumbine, R., Liu, Q., and Lu, C.-H.: Impacts of aerosols on
643 meteorological assimilation: Aerosol impact on simulated brightness temperature and
644 analysis fields. *JCSDA Quarterly*, 66, Spring 2020, <https://doi.org/10.25923/4pt1-wx36>,
645 2020.

646 Wei, S.-W., Lu, C.-H., Liu, Q., Collard, A., Zhu, T., Grogan, D.F.P., Li, X., Wang, J., Grumbine
647 R., and Bhattacharjee, P.: The impact of aerosols on satellite radiance data assimilation
648 using NCEP global data assimilation system. *Atmosphere*, 12(4), 432,
649 <https://doi.org/10.3390/atmos12040432>, 2021.

650 Wilcox, E.M., Lau, K.M., and Kim, K.Y.: A northward shift of the North Atlantic Ocean
651 Intertropical Convergence Zone in response to summertime Saharan dust outbreaks.
652 *Geophys. Res. Lett.*, 24, L04804, <https://doi.org/10.1029/2009GL041774>, 2010.

653

654

655

656

657

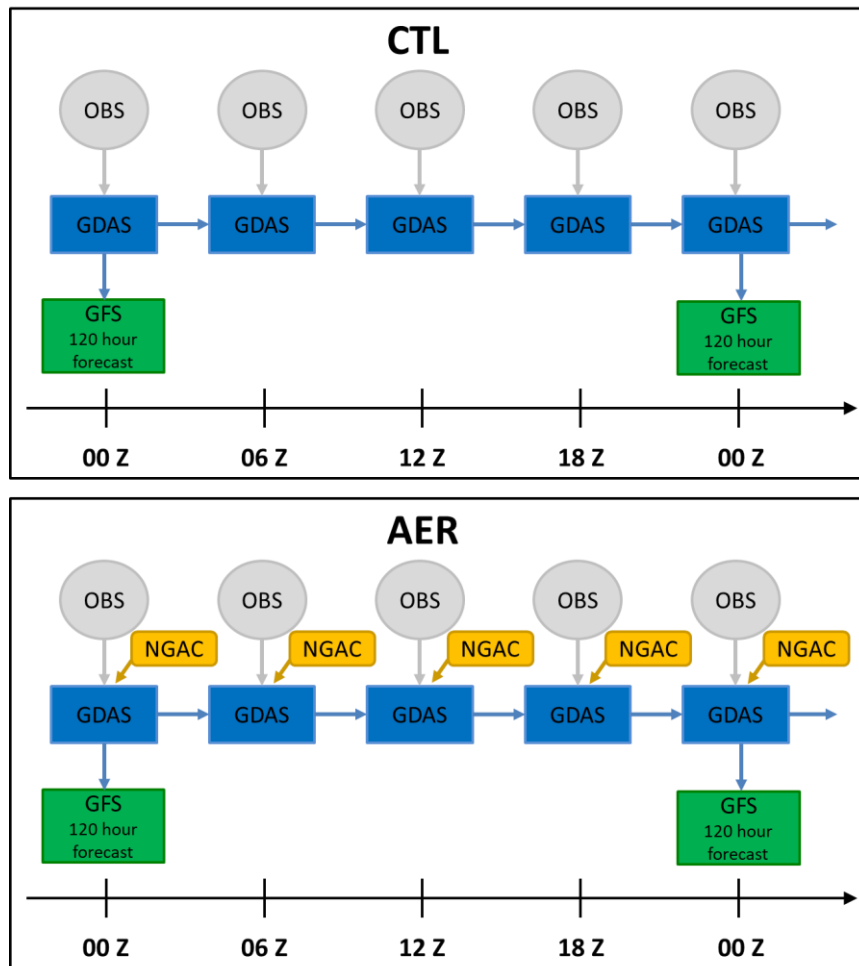
658

659

660

661

662



663

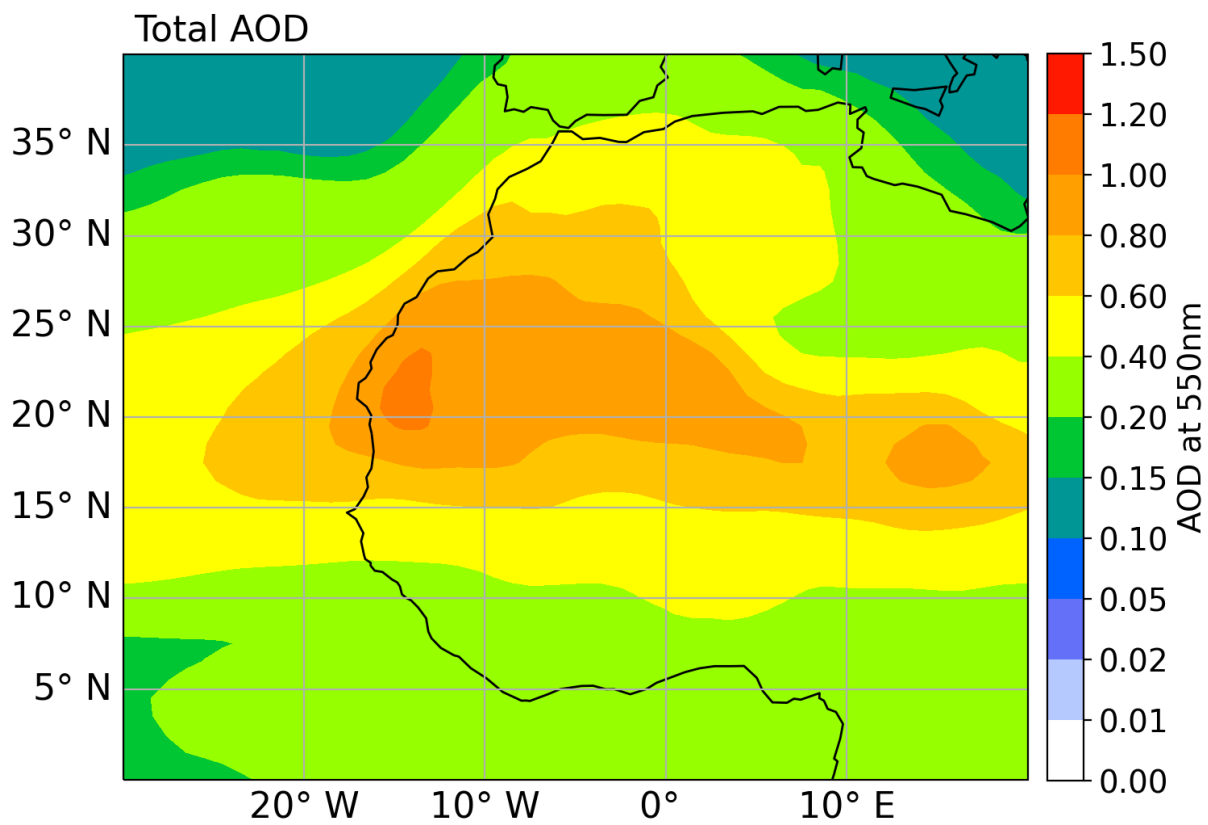
664

665

666

667

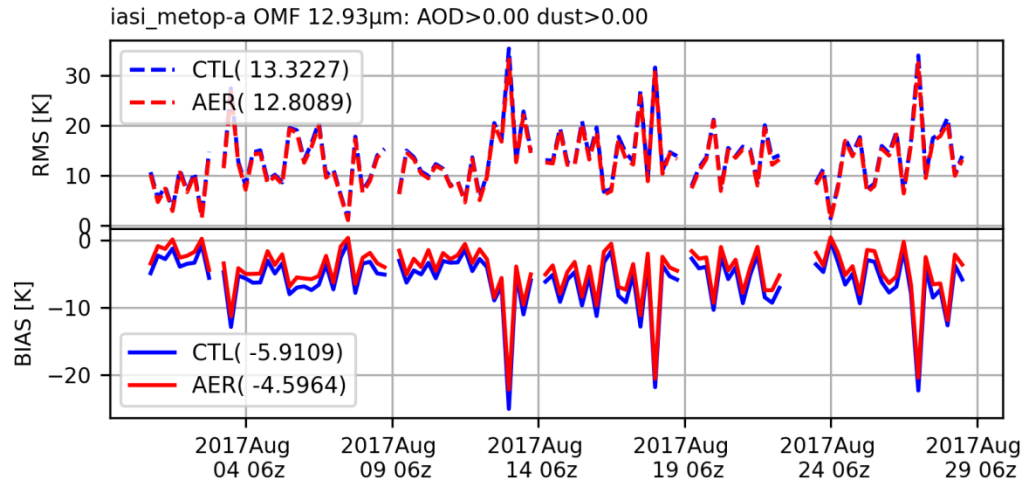
Figure 1. Schematic flow chart of the aerosol-blind (CTL) and aerosol-aware (AER) experiments in this study. See text for details.



668

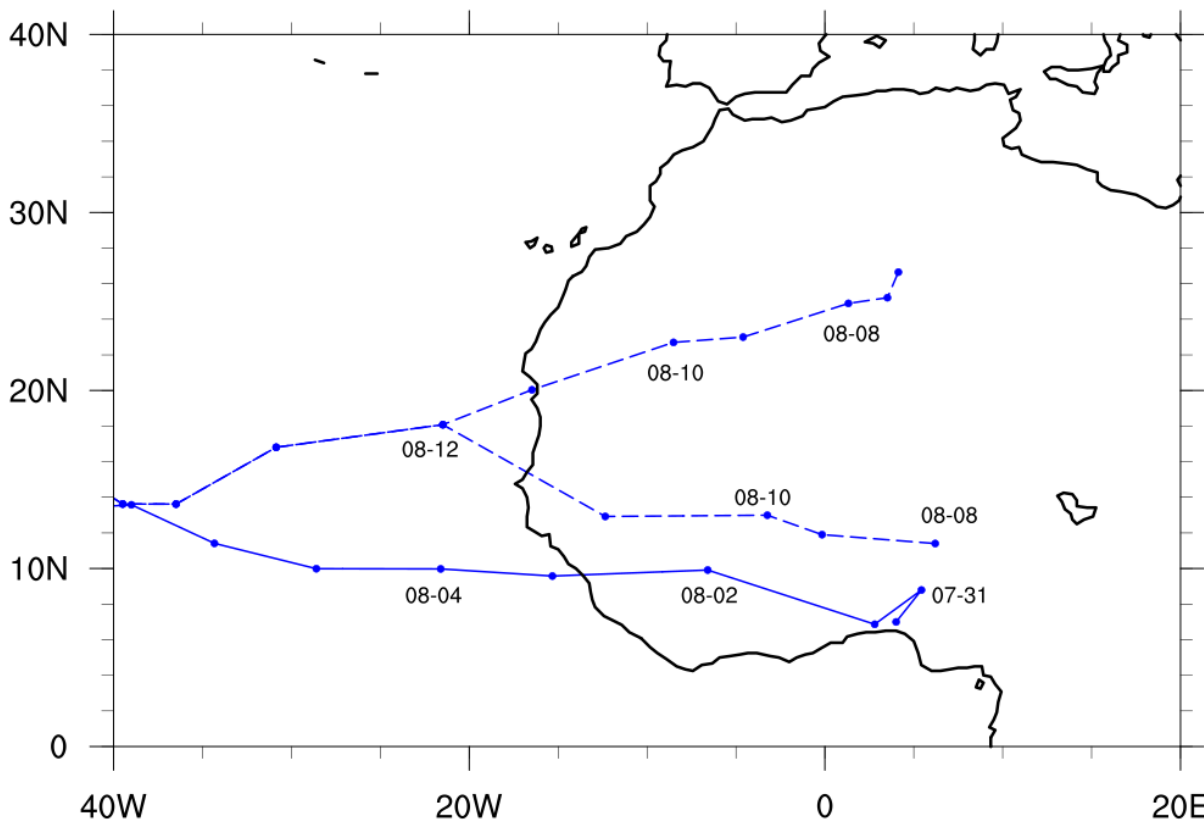
669 **Figure 2.** Total Aerosol Optical Depth (AOD) from the NGAC forecasts, averaged over August 1st-28th, 2017.

670



671

672 **Figure 3.** Statistics for the averaged observation-minus-forecast (OMF) infrared brightness temperatures (IR BT) (12.93 μ m)
 673 from the IASI hyperspectral sensor from CTL (red) and AER (blue). The timeseries includes all observations over the region (0-
 674 40°N, 20°E-30°W), irrespective of aerosol loading. The numbers in the legend are the mean statistics.
 675



676

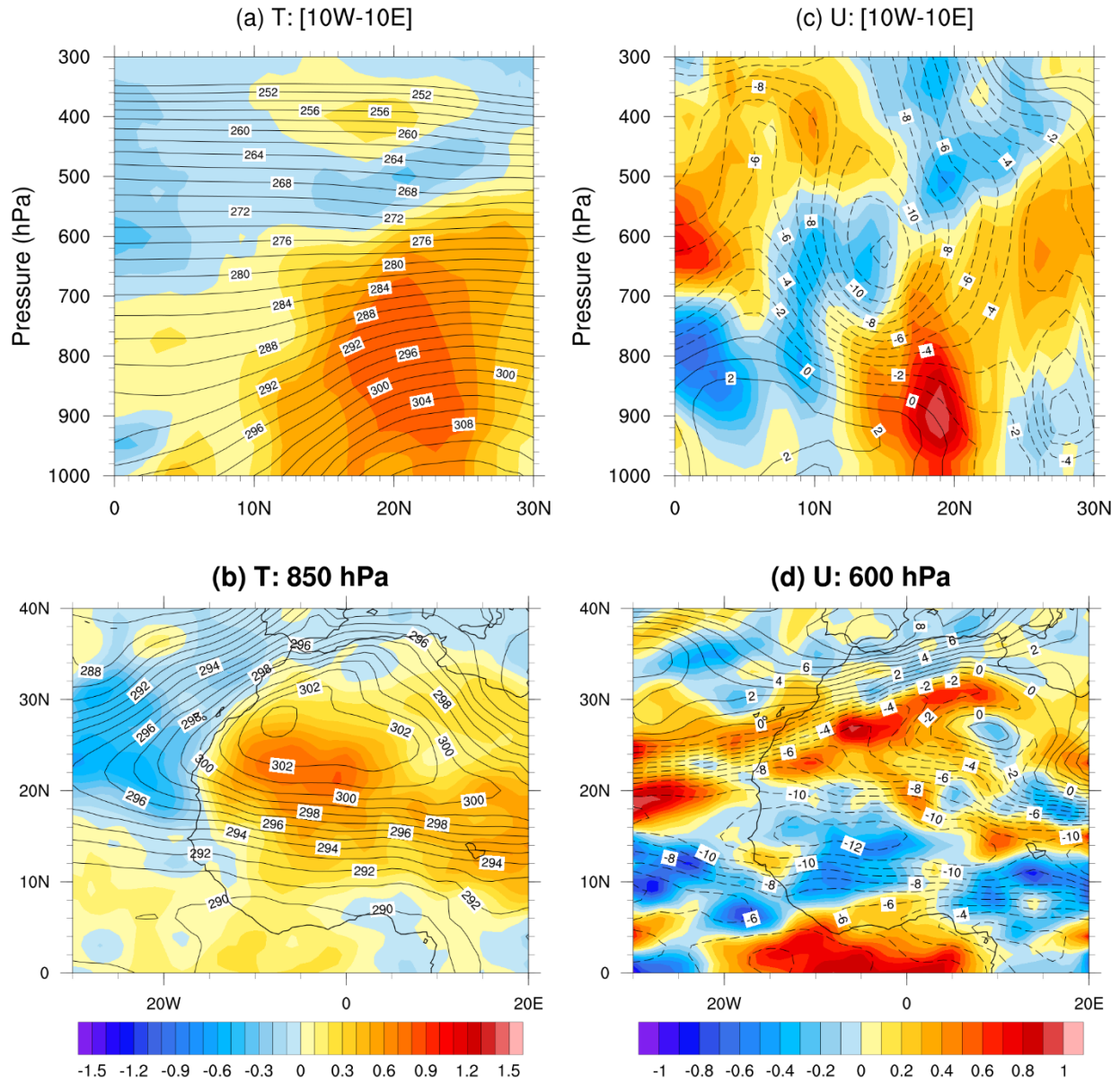
677

678

679

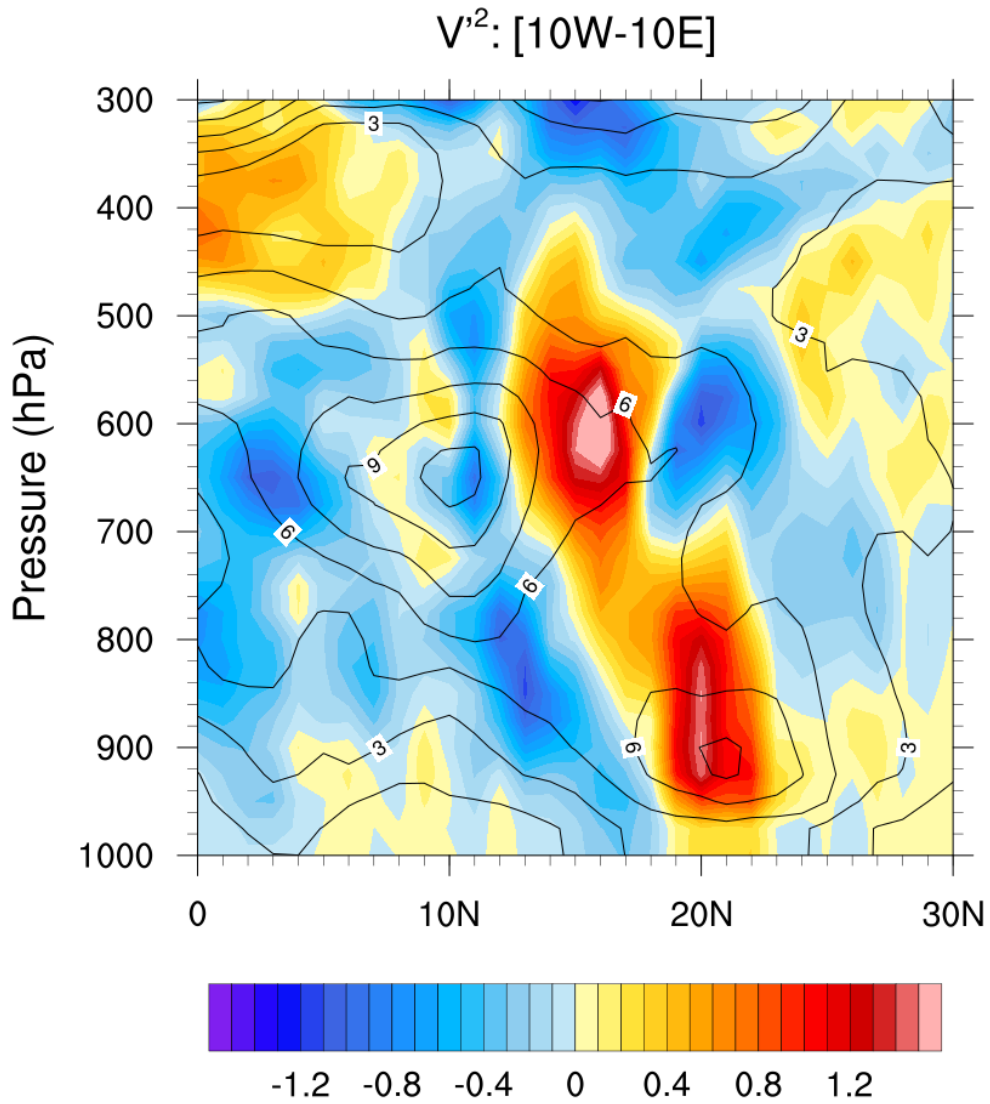
680

Figure 4. Daily locations (at 00 UTC) of the AEWs corresponding to Gert (solid) and Harvey (dashed) obtained by the tracking algorithm in the CTL run (time period: August, 2017).



681

682 **Figure 5.** Vertical and horizontal cross sections of the CTL analysis (contours) and the AER – CTL analysis difference (colors)
 683 for (a, b) temperature, T, and (c, d) zonal wind, U. The vertical sections (top) are zonally-averaged from 10°W – 10°E, while
 684 horizontal sections (bottom) are taken at specified pressure levels. Contour/color units: (a,b) K and (c,d) ms⁻¹. The fields are time-
 685 averaged from August 1st – August 28th, 2017.
 686



687

688 **Figure 6.** Time-averaged 2-6 day filtered meridional wind variances, v'^2 , of the CTL analysis (contours) and the AER – CTL
 689 analysis difference (colors) zonally-averaged from 10°W – 10°E for August, 2017. Contour/color units: m^2s^{-2} .
 690

691

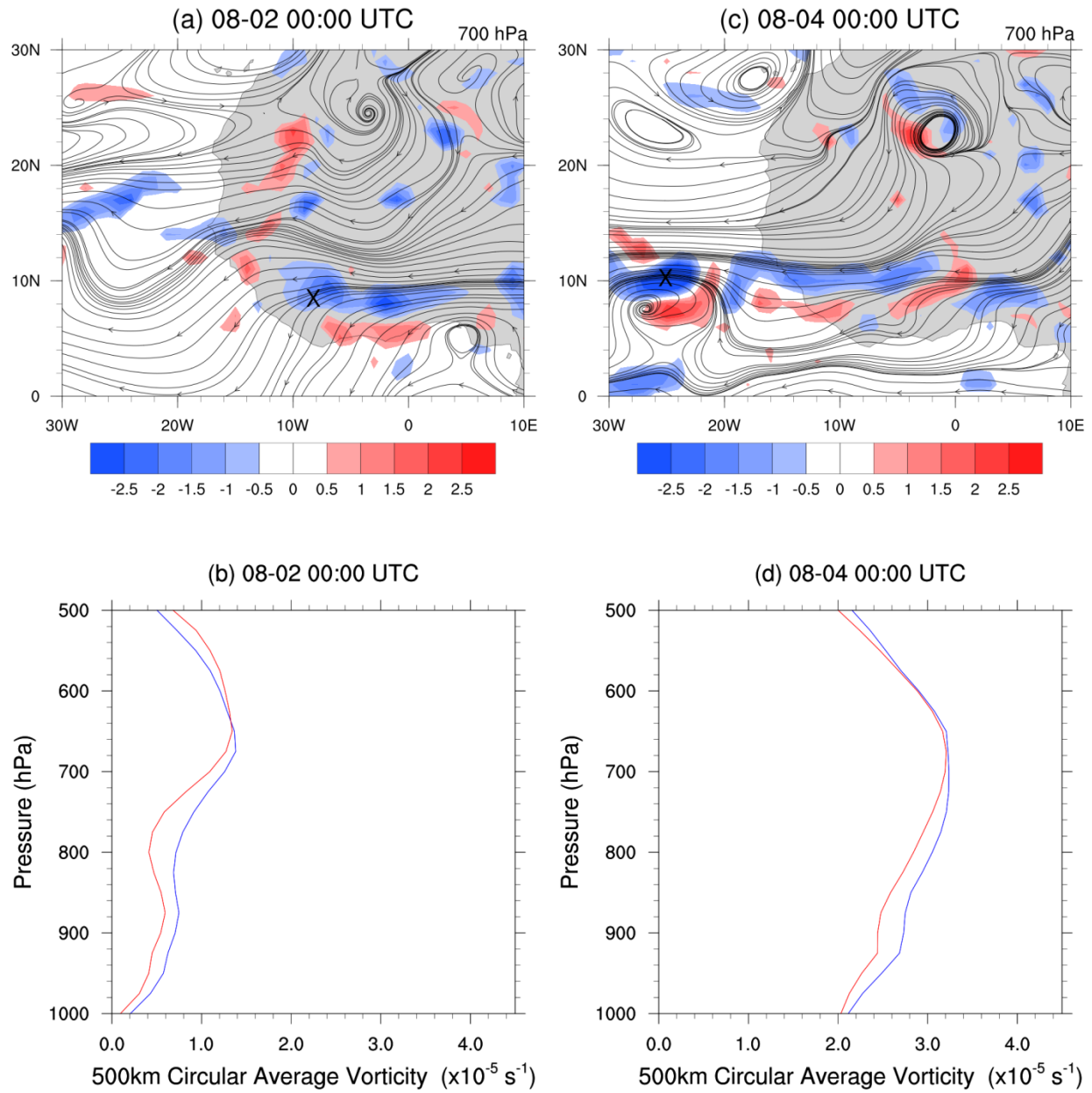
692

693

694

695

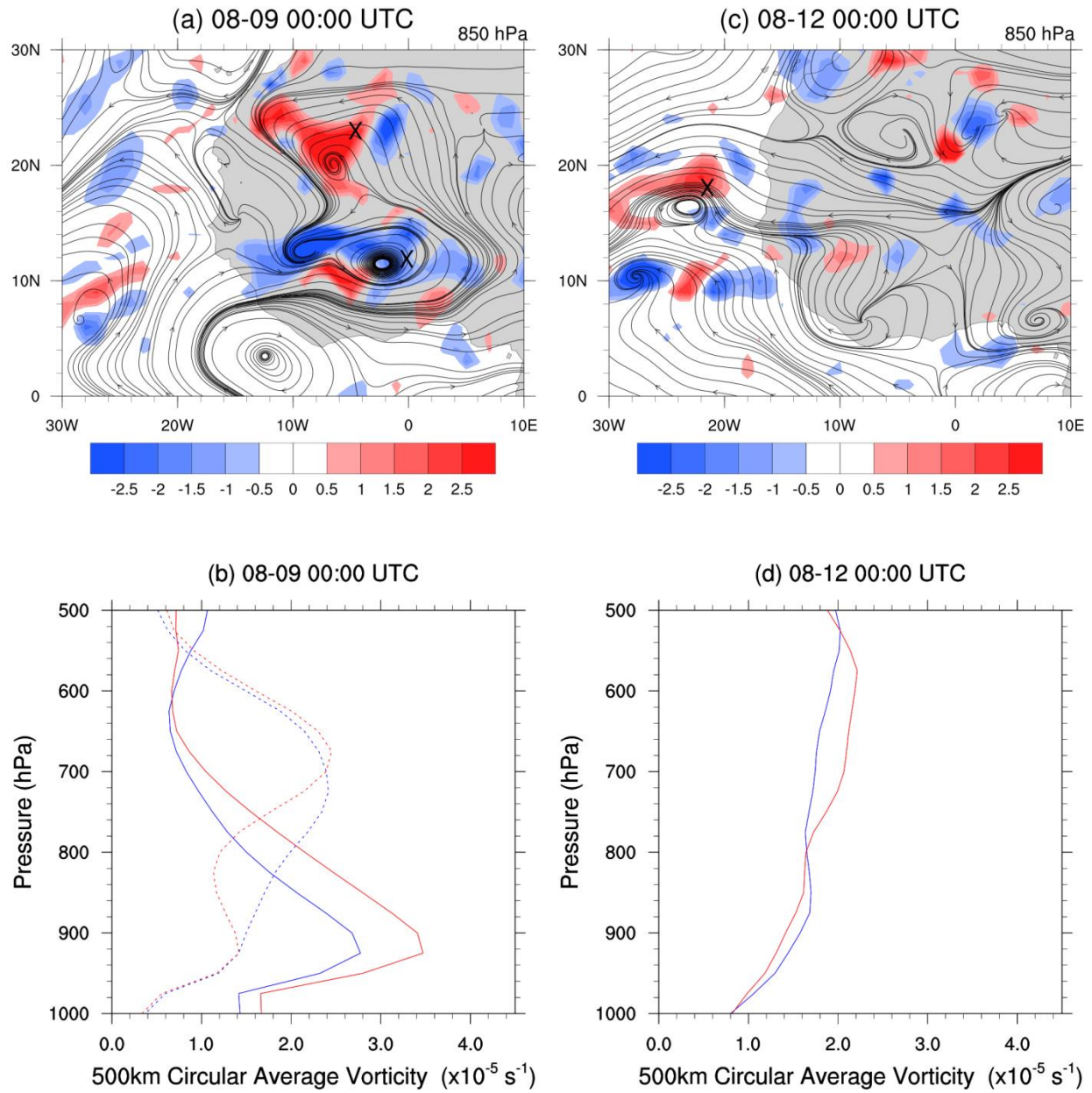
696



697

698
699
700
701
702
703

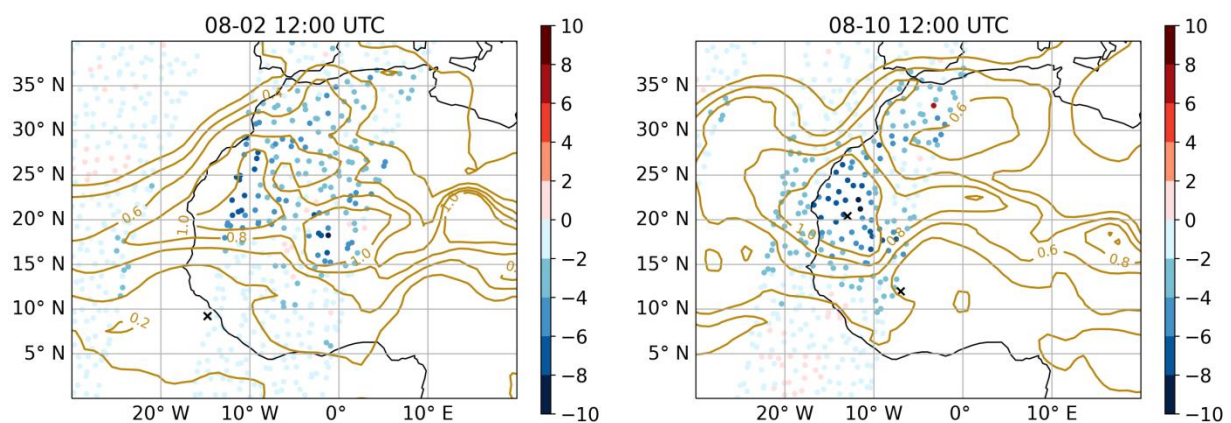
Figure 7. The evolution of the AEW associated with Gert on Aug 2nd (left) and Aug 4th (right). The top panels show the 700 hPa CTL streamlines (black) and the AER - CTL 700 hPa cyclonic vorticity differences (red/blue); the 'X' marks the wave's location from the tracking algorithm. The bottom panels show the circular average vorticity (radius 500 km) taken at the X's for CTL (blue) and AER (red).



704
705
706
707
708
709

Figure 8. As in Fig. 7, but for the evolution of the AEW associated with Harvey on Aug 9th (left) and Aug 12th (right) The horizontal plots (top) show 850 hPa CTL streamlines and 850 hPa AER-CTL cyclonic vorticity differences, instead of 700 hPa, to better capture the two-circulation signal. Over Africa (b), we overlay the vertical vorticity structures of the northern (solid) and southern (dotted) circulation for CTL (blue) and AER (red).

710



711
 712 **Figure 9.** AER – CTL differences in simulated BT at 12.93 μ m from the IASI (colored circles) with the NGAC AOD (brown
 713 contours) on August 2nd, 12:00 UTC (left) and Aug 10th, 12:00 UTC (right). The X's mark the location of the wave centers for
 714 the AEW that developed Gert (left: 8°N,14°W) and Harvey (right: at 12°N,17°W and 20.5°N,13°W). Colorbar units: °K.
 715

716
 717
 718
 719
 720
 721
 722

Gert

Initialization	1 day	2 day	3 day	4 day	5 day
July 31 st	0.13	0.21	0.19	0.38	0.03
August 1 st	0.17	0.27	0.25	0.10	0.08
August 2 nd	0.19	0.04	0.24	0.10	0.08
August 3 rd	0.06	0.20	0.23	0.09	1.02

Harvey

Initialization	1 day	2 day	3 day	4 day	5 day
August 8 th	0.23	0.05	0.23	0.32	0.27
August 9 th	0.08	0.07	0.06	0.33	0.32
August 10 th	0.35	0.32	0.17	0.31	0.49
August 11 th	0.22	0.39	0.49	0.46	0.64

724
725
726
727
728
729

Table 1. RMSE relative differences in the 1000 – 500 hPa relative vorticity between the AER and CTL forecasts for the AEWs that developed Gert and Harvey. For each forecast day, the relative differences are calculated by taking (AER-CTL)/CTL of the RMSEs over the region following the AEWs (see text for more details). The green values indicate AER improved the forecast, while red values indicate AER degraded the forecast; crossed-out values were not significant to the 99% confidence interval. The staircase border in each case separates times when the waves are located onshore (upper left) and offshore (lower right).